



Exciton dissociation and transfer behavior and surface reaction mechanism in Donor–Acceptor organic semiconductor photocatalytic separation of uranium

Zifan Li^a, Zhibin Zhang^{a,*}, Xiang Zhu^a, Cheng Meng^{a,*}, Zhimin Dong^a, Songtao Xiao^b, Yingcai Wang^a, Youqun Wang^a, Xiaohong Cao^a, Yunhai Liu^{a,*}

^a State Key Laboratory of Nuclear Resources and Environment, East China University of Technology, Nanchang, Jiangxi 330013, PR China

^b Department of Radiochemistry, China Institute of Atomic Energy, Beijing 102413, PR China

ARTICLE INFO

Keywords:

Uranium
Separation
G-C₃N₄
Photocatalytic
Photocatalytic-induced-uranyl-coordination-reaction (PIUCR)

ABSTRACT

Photocatalytic uranium extraction from nuclear effluent is a promising approach for avoiding environmental damage and recovering uranium resources. Here, a hollow tube-like D-A organic semiconductor photocatalyst consisting of triazine (Acceptor) and carbon ring (Donnor) was synthesized via two cheap monomers, sodium alginate and melamine. The incorporation of carbon ring structure could endow g-C₃N₄ with unique hollow hexagonal tube-like morphology, modulate the electronic excitation model, lower the energy for exciton dissociation, and promote the adsorption and activation of O₂. Thus, the D-A photocatalyst established high efficiency of photocatalytic uranium separation under LED light and high concentration of anions and cations interference. More importantly, we propose a novel theory, that photocatalytic-induced-uranyl-coordination-reaction (PIUCR), and highlight that the formation rate and pathway of crystal nucleus is the most crucial step for the surface reaction of photocatalytic uranium separation. This study provides insights and guidelines for the in-depth understanding of the photocatalytic separation of uranium.

1. Introduction

The uranium photocatalytic separation strategy has received considerable interest because it can substantially convert soluble U(VI) into insoluble uranium oxides, allowing for subsequent isolation of U(VI) from an aqueous solution [1–5]. Lately, graphitic carbon nitride (g-C₃N₄, CN) has sparked great attention and research as a low-cost photocatalyst for uranium extraction from seawater or nuclear effluent [6–8]. Nevertheless, the vivid photocatalytic reaction driven by CN continues to be limited by its inadequate photocatalytic properties. Customarily, the photocatalytic process involves three basic steps, including light harvesting, photogenerated electron and hole separation and migration, and surface reaction [9,10]. Therefore, several strategies, such as doping elements [11], and regulating morphology [12] have been taken to enhance light harvesting, or improve crystallinity [13], introduce defects [14], and construct heterojunctions to promote the migration of electron and hole [15,16]. In addition, improving the BET and hydrophilicity of the material also facilitates the photocatalytic surface reaction [17]. However, a few studies have reported the

optimization of the above three steps by a simple modification, because an overly complex modification strategy can make CN lose its cheap advantage. Furthermore, most current studies about photocatalytic reactions only focus on light harvesting or carrier migration. The efforts dedicated to separating coulomb-interacted bound electron-hole pairs and the surface reaction of photocatalytic separation of U(VI) are somewhat limited.

For the hydrogen evolution or CO₂ reduction reaction, the first step of surface reaction mainly contained the adsorption of H⁺ or CO₂ on the electron-rich reactor sites. After that, the adsorbed H⁺ and CO₂ received photoelectrons to form H₂ or CO [18,19]. Based on these mature research mechanisms, the surface reaction of photocatalytic separation of U(VI) should be the same, that is, the adsorbed U(VI) receive photoelectrons to reduce into U(IV) [20]. However, the inferential mechanism cannot explain many experimental phenomena, such as the final products of uranium in many photocatalytic reactions are studtite ((UO₂)(O₂)·2 H₂O), a kind of U(VI) contained uranium oxide, rather than UO₂ [3,21–24]. Adding oxygen to the uranium solution can accelerate photocatalytic uranium separation [25]. Several necessary

* Corresponding authors.

E-mail addresses: zhbzhang@ecut.edu.cn (Z. Zhang), mengchengperfect@126.com (C. Meng), yhliu@ecut.edu.cn (Y. Liu).

<https://doi.org/10.1016/j.apcatb.2023.122751>

Received 12 February 2023; Received in revised form 6 April 2023; Accepted 9 April 2023

Available online 11 April 2023

0926-3373/© 2023 Elsevier B.V. All rights reserved.

researches have confirmed that H_2O_2 play an essential role in the photocatalytic separation of U(VI), which can react with U(VI) to form studtite [26,27]. Obviously, the complex coordination environment of uranyl in solution during the photocatalytic reaction has not received sufficient attention in the last decade.

Herein, we have synthesized a Donnor-Acceptor type hollow tubular g-C₃N₄ using two inexpensive monomers, sodium alginate (SA, Donnor, \$11.21/kg) and melamine (MA, Acceptor, \$1.20/kg), for the purpose of photocatalytic separation of U(VI) and investigation of reaction mechanism. The carbon ring structure introduced by sodium alginate widens the absorption spectrum and enhances the built-in electric field of CN molecules, further promotes charge separation from volume and surface in the photocatalyst, and finally achieves efficient photocatalytic separation of U(VI) under LED illumination with a high separation rate of 646 $\mu\text{mol}/(\text{g}\cdot\text{h})$. More importantly, this work proposes an interesting photocatalytic separation mechanism for uranium, photocatalytic-induced-uranyl-coordination-reaction (PIUCR), and verifies this mechanism through a reasonable design of various unusual photocatalytic experiments and tracking of active substances in photocatalytic reactions. The universality of this mechanism is further demonstrated by combining multiple photocatalytic materials and different photocatalytic reaction conditions. This article emphasizes that the reaction conditions for photocatalytic separation of U(VI) will greatly affect the mechanism of U(VI) separation, with surface photocatalytic reactions of the photocatalyst being the most important. This work provides guiding principles for the construction of new photocatalysts for photocatalytic separation of U(VI), and the proposed mechanism is expected to generate new separation technologies for the selective separation and recovery of uranyl ions from solution.

2. Experimental section

2.1. Materials synthesis and characterization

The synthesis of bulk g-C₃N₄ (BCN), precursor of g-C₃N₄, carbon ring conjugated hollow tube g-C₃N₄ (HCNCR), hollow tube g-C₃N₄ (HCN), cadmium sulfide (CdS), anatase titanium dioxide (TiO₂), COF-1, COF-2, and UiO-66 are listed in the Supporting Information Text S1. All reagents were obtained from Aladdin Industrial Inc. Deionized (DI) water was used throughout. The detailed characterization information is exhibited in Text S2.

2.2. Computational details

The B3LYP density functional was used for all Density Functional Theory (DFT) and the CAM-B3LYP density functional for Time Dependent-Density Functional Theory (TD-DFT) calculations, together with the 6–31 G(d) basis set using Gaussian 16 software [28]. The adsorption energy of O₂ (ΔE_{ads}) was computed by M062X/def2TZVP according to formula (1), where $E_{\text{sub}+\text{O}_2}$ is the calculated total energy of the adsorption system, E_{sub} is the calculated energy of the photocatalyst, and E_{O_2} is the calculated energy of the O₂ molecule.

$$\Delta E_{\text{ads}} = \Delta E_{\text{sub}+\text{O}_2} - \Delta E_{\text{sub}} - \Delta E_{\text{O}_2} \quad (1)$$

Semiclassical dispersion corrections were with GD3BJ in all calculations. The solvation effect of water was accounted for using the PCM/SMD solvation model. The electron distributions at these exciting statuses and the electron localization function (ELF), density of states (DOS), and partial DOS (PDOS) were obtained with Multiwfn [29–31] and Vesta.

2.3. Photocatalytic tests

The photocatalytic experiments were performed in a 100 mL quartz sandwich reactor cooled with circulating water at the temperature of 20 \pm 0.2 $^{\circ}\text{C}$. Specifically, 10 mg of photocatalysts were mixed with 50 mL

uranium solution ($\text{C}=50 \text{ mg/L}$, containing 5% methanol). pH= 5.0 was achieved by adding trace HNO_3 (0.01 mol/L) or Na_2CO_3 (0.01 mol/L) solutions to the uranium solution. The mixture was stirred in the dark for 60 min before being illuminated with a 420 nm LED light. A 0.22 μm membrane was used to filter 1.0 mL of the solution after a specific time. The concentration of UO_2^{2+} was determined at 650 nm by using the Arsenazo-III method through a UV–vis spectrophotometer. The removal rate of U(VI) can be calculated as C_t/C_0 , that C_0 and C_t are the initial concentrations of U(VI) and the concentrations at a time (t).

3. Results and discussion

3.1. Material synthesis and characterizations

Melamine was first hydrolyzed into precursor of hydrogen-bonded cyanuric acid-melamine (CM), with the assistance of recrystallization and hydrothermal processes [32]. After that, the precursor was heated at 550 $^{\circ}\text{C}$ to form hollow tube g-C₃N₄ (HCN). The graphitic carbon ring conjugated hollow tube g-C₃N₄ (HCNCR) was synthesized with a designed quantity of sodium alginate added. The contrasted bulk g-C₃N₄ (BCN) was synthesized by treating melamine at 550 $^{\circ}\text{C}$ for 3 h. The hydrophilicity of the acquired HCNCR was enhanced, as demonstrated in the contact angle assessments (Fig. S1). The HCNCR showcased admirable dispersibility in water, accompanied by a distinct Tyndall effect, and no sediments were discernible following basic sonication, while BCN evidenced multiple precipitates (Fig. S2). This augmented hydrophilicity and dispersibility of HCNCR assisted the photocatalytic reaction when executed in an aqueous solution.

The formation process of HCNCR was studied in detail by a series of characterizations. The XRD pattern displays that the precursor of CM exhibits a high degree of crystallinity (Fig. S3). After polymerized under 550 $^{\circ}\text{C}$, the (002) diffraction corresponding to the interlayer stacking of aromatic rings shifted from 27.9 $^{\circ}$ of precursor to 27.3 $^{\circ}$ of HCN (Fig. 1a and S3), confirming that the interlayer spacing of precursor was expanded. Meanwhile, the BET surface areas and volume of HCN and HCNCR were significantly dilated (Fig. 1b), which suggests that the precursor was efficiently exfoliated by cooccurring thermal exfoliation and self-assembly to form a quadrangular nanotube structure (Fig. 1c). With the addition of carbon ring-contained sodium alginate, the XRD tests show a reduction in the intensity of the (002) peak (Fig. 1a), indicating a slight decrease in the crystallinity of HCNCR, while still preserving it for the most part. This suggests that the addition of a carbon ring had an insignificant impact on the molecular structure of CN. Interestingly, the addition of sodium alginate affected the self-assembly behaviour of CM supermolecules because of the appearance of H bonds, leading to the morphology of precursor remodelling from quadrangular tubes into hexagonal tubes (Fig. S4), thus resulting hexagonal hollow tube HCNCR after polymerized under high- temperature (Fig. S5). The decreased internal angle of the polygonal CNCR effectively enhances the utilization of incident light through multiple reflections, thereby facilitating a higher photocatalytic uranium separation potency.

Under high-resolution TEM (HRTEM) observation, the lattice fringes of 0.212 nm appointed to (100) planes of graphite and the (100) plane of the 3-s-triazine (0.238 nm) are founded (Fig. 1e and 1f) [33,34]. Moreover, Raman spectra (Fig. S6) also verify the broad D and G bands (1344 and 1587 cm^{-1}) assigned to the characteristic structure of graphite [35]. Element analysis and XPS spectra further analyzed the element content and valence information about the surface. The atomic ratio of C/N in HCNCR is 1.04 (approximately C_{4.2}N₄), which is significantly higher than that of HCN (Table S1). Besides, owing to the abundance of carbon ring, graphite sp² C (284.8 eV) signals took up to 27% of C1s peak in HCNCR (Fig. S7). Combining the above results, we tend to contemplate that the HCNCR has been successfully modified by the in-plane incorporated carbon ring.

The optical property and electronic structures of the samples were characterized. As shown in UV–vis diffuse reflectance spectra (Fig. 2a),

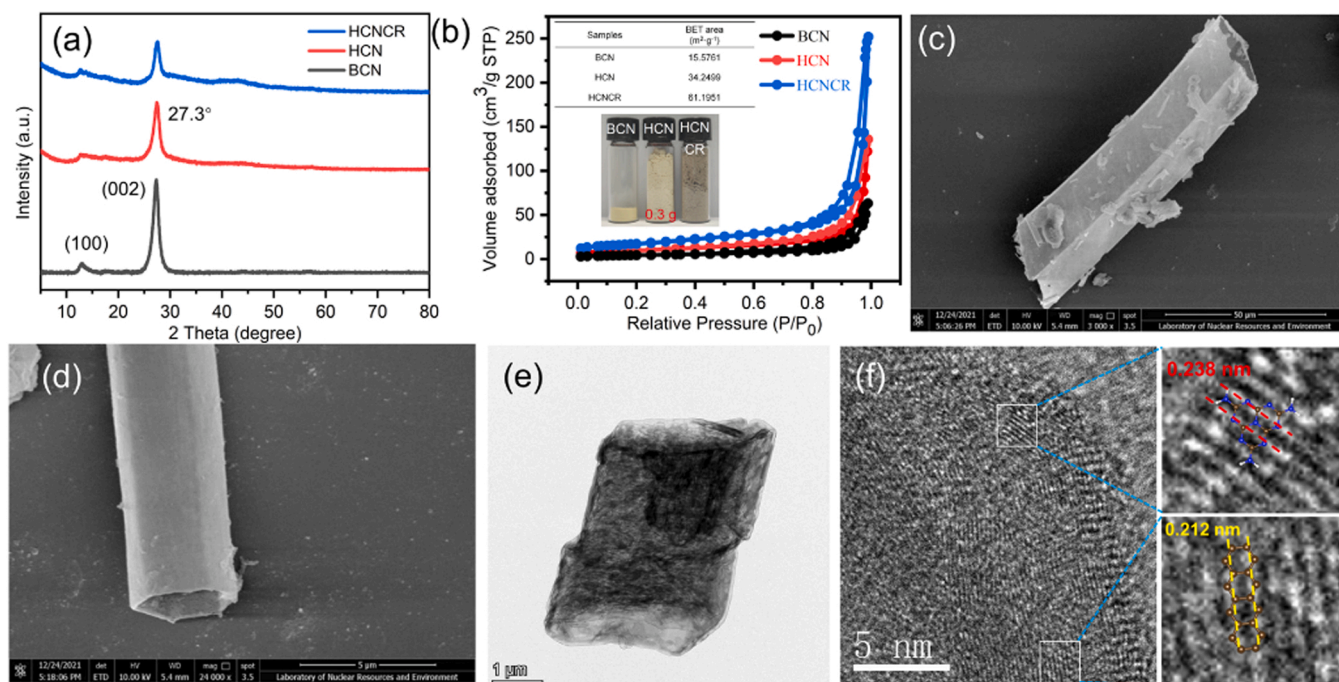


Fig. 1. (a) XRD pattern of BCN, HCN and HCNCr. (b) N_2 -sorption isotherms of BCN, HCN and HCNCr (inset: BET surface area and the photographs of 0.3 g BCN, HCN and HCNCr). The SEM images of (c) HCN and (d) HCNCr. (e) TEM image and (f) HRTEM image for HCNCr.

BCN and HCN reveal a prominent absorption edge at around 450 nm, whereas another extended optical absorption band at 450–800 nm are observed in HCNCr, which is mainly attributed to the high optical transparency of carbon ring [36]. This is consistent with the apparent color of photocatalysts deepening from light yellow (BCN) to oxford gray (HCNCr) (Fig. S8). Moreover, according to the transformed Kubelka–Munk function and XPS VB spectra (Fig. S9), the bandgaps, the valence bands and conduction bands of HCNCr can be determined to be 1.87 eV, 1.14 eV and -0.73 eV (vs. NHE), with the specific band structure comparison displayed in Fig. 2b.

3.2. Photocatalytic performance toward uranium separation

The photocatalytic uranium-separation experiments were performed under LED light irradiation ($\lambda > 420$ nm). As shown in Fig. 2c, BCN establishes poor photocatalytic activity. With facile regulating the microstructure of CN into hollow tube structure, the photocatalytic uranium-separation rate is remarkably enhanced and further improved once incorporating carbon ring. The calculated photoreaction rate of HCNCr is $646 \mu\text{mol}/(\text{g}\cdot\text{h})$, and the performance comparison with the reported literatures are list in Table S2. Notably, under sunlight irradiation, the photocatalytic activity of HCNCr remains a consistent pattern when exposed to LED light (Fig. S10). The improved photocatalytic activity of HCNCr can be attributed to the distinctive morphology of hexagonal nanotubes, which enlarges the BET surface area of photocatalysts, exposing more reactive sites and reflecting incident light to enhance the utilization of sunlight. In addition, the optimum electronic band structures are more favorable to photocatalytic uranium separation.

Finally, the effect of ionic strength and cycling tests were conducted, which are significant indicators in determining the practical viability of the photocatalyst. As displayed in Fig. 2d, e, Although the presence of high concentrations of NaCl and NaSO_4 (0.25 M), two typical impurities found in mine wastewater [21], led to a decrease in the separation rate, the U(VI) uptake capacities of HCNCr were only slightly affected. Moreover, after five sequential runs, the photocatalytic separation of U(VI) over HCNCr is well retaining (Fig. 2f), and the morphology,

structure and chemical composition of the photocatalyst keep almost unaffected (Fig. S11 and Table S3). These results indicate that the HCNCr sample possesses outstanding photocatalytic reusability and stability, demonstrating the robust effect of microstructure regulation and carbon ring incorporation on photocatalytic activity.

3.3. Photoelectrochemical characterization and DFT calculation

Photocurrent tests and electrochemical impedance spectroscopy (EIS) were carried out to comprehend the activity-structure relationship in depth. Under LED light irradiation, the photocurrent results demonstrate the highest and medium density for HCNCr and HCN, respectively (Fig. 2g). This confirms the increased amount of photogenerated carriers and reduced resistance at the solid-solution interface. These results are further supported by the fact that, according to the EIS measurements, HCNCr and HCN exhibit a smaller radius of a semicircle than that of BCN (Fig. S12). To clarify the D-A characteristics of HCNCr, DFT calculation was performed with simplified fragments. The structures of 3CN (three triazine units) and CNCr (three triazine units and carbon ring) are displayed in Fig. S13. As shown in Fig. 2h and S14, the gap between the highest occupied molecular orbital (HOMO) and lowest unoccupied molecular orbital (LUMO) locations of CNCr (1.86 eV) is much lower than that of 3CN (4.25 eV). The HOMO-LUMO distribution of CNCr is more broader, indicating that the incorporation of a carbon ring can enhance the electroconductivity of the photocatalyst and decrease the energy required for electron excitation [37]. This is in agreement with the characterization conclusions mentioned above.

Subsequently, the separation efficiency of photo-induced carriers and the carrier-transfer dynamics of the samples were evaluated by using steady-state and time-resolved photoluminescence (PL and TRPL) spectroscopy. As displayed in Fig. S15, the PL peak intensity gradually decreased with microstructure regulation and carbon ring incorporation, indicating that a lower recombination rate of the photo-induced carriers exists in HCN and HCNCr. These results are consistent with the facts observed in TRPL spectroscopy (Fig. 2i). Both HCN and HCNCr establish longer radiative lifetimes (τ), 31.34 ns and 44.76 ns, respectively, while 19.88 ns for that of BCN. In general, longer radiative

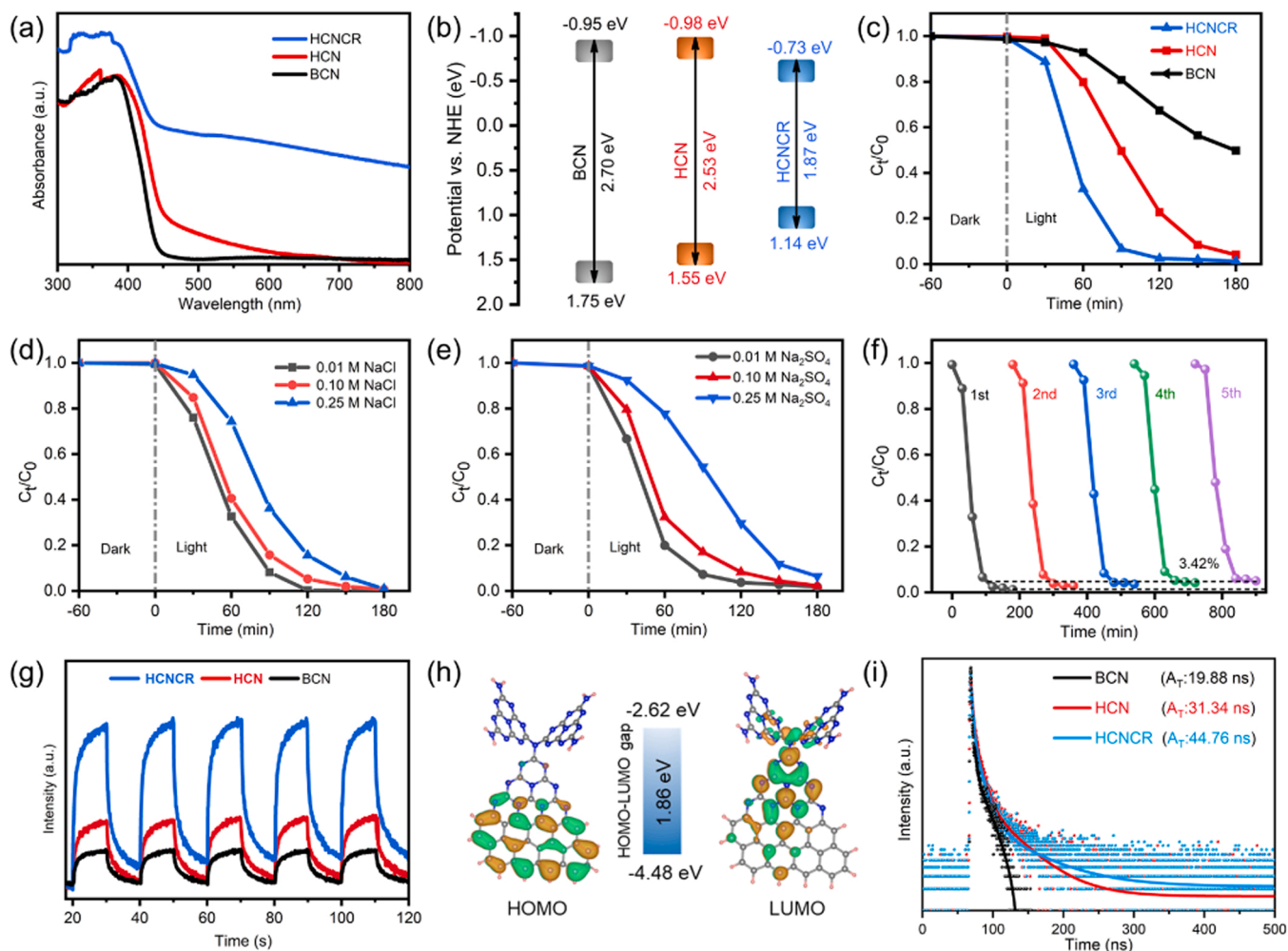


Fig. 2. (a) UV-vis diffuse reflectance spectra and (b) Band structure for BCN, HCN, and HCNCr. (c) Time course of photocatalytic U(VI) separation under LED light irradiation. Influence of various competitive ions (d) NaCl and (e) Na_2SO_4 . (f) Cycling tests over HCNCr. (g) Photocurrent measurements for BCN, HCN, and HCNCr. (h) The distribution of HOMO and LUMO wave functions of CNCR. (i) Time-resolved fluorescence decay spectra of prepared samples.

lifetimes provide a greater chance for photogenerated charges to participate in photocatalytic reactions before being quenched [38].

3.4. TD-DFT calculation and exciton dissociation behavior

Polymeric semiconductors, which inherently possess low dielectric characteristics, have a high exciton binding energy (E_b). This leads to bound electron-hole pairs or excitons dominating photoexcitation processes, rather than free carriers [39]. Thus, the influences of exciton dissociation, the primary step in the photocatalytic reaction, ought to be systematically considered. Here, time dependent-density functional theory (TD-DFT) calculations have been carried out to study the effect of carbon ring on the internal electric field (IEF) and exciton dissociation of 3CN. For both 3CN and CNCR, the excited states of $S_0 \rightarrow S_1$ have the strongest oscillator strength, where two electronic excitation bands located at 330 nm and 662 nm, respectively (Tables S4 and S5). In one triazine unit, the electrons are mainly distributed on the C atoms, bridge N atoms and inner N atoms, whereas the holes are leaned against the triangular edge N atoms (Fig. S16a-c). The charge density difference (CDD) confirmed the photogenerated electrons-holes pairs could be effectively delocalized at the atom level (Fig. S16d). Unfortunately, for 3CN, the separation of hole/electron remains similar situation with one triazine unit (Fig. S17). As displayed in the total density of states (TDOS), the VB and CB of 3CN are mainly originated from the triangular edge N atoms and C atoms, respectively and the projected density of

states (PDOS) for each triazine unit are precisely alike (Fig. 3a, b). The above calculations suggest that polymeric CN behaves more like a monomer than an inorganic semiconductor, and the transport of photo-induced carriers between different triazine units is impossible in polymeric CN. Upon incorporating the carbon ring, the valence band (VB) of CNCR is primarily occupied by the in-plane carbon ring, while the conduction band (CB) is composed of both carbon ring and three triazine units (Fig. 3c). This suggests that the triazine units act as an acceptor, while the carbon ring exhibits excellent electron-donating properties (D-A feature), which is further confirmed by CDD of CNCR (Fig. 3g). The influences of carbon ring on the IEF in 3CN have also revealed by high excited states of CNCR. As shown in the Fig. S18, the introduction of the carbon ring caused the electrons to mainly distribute in C_3N_4 unit frag.3, while the holes distributed in C_3N_4 unit frag.1 and C_3N_4 unit frag.2. Additionally, the PDOS of three triazine units are notably different, indicating that polymeric CN is no longer a monomer and that more efficient charge separation and transport can be achieved (Fig. 3d). The region of density depletion (blue) and the density increment zones (yellow) represent instance discretization on a three-dimensional (3D) grid around the molecule. The spatial distance between the two barycenters of density distributions can be defined as D_{CT} , the excitation length of charge transfer [40]. As shown in Fig. 3f and 3 h, for the 3CN model, the shapes of density depletion and density increment zones look closer to circular, and are overlapped entirely, indicating the ductility of the distribution of holes and electrons in each

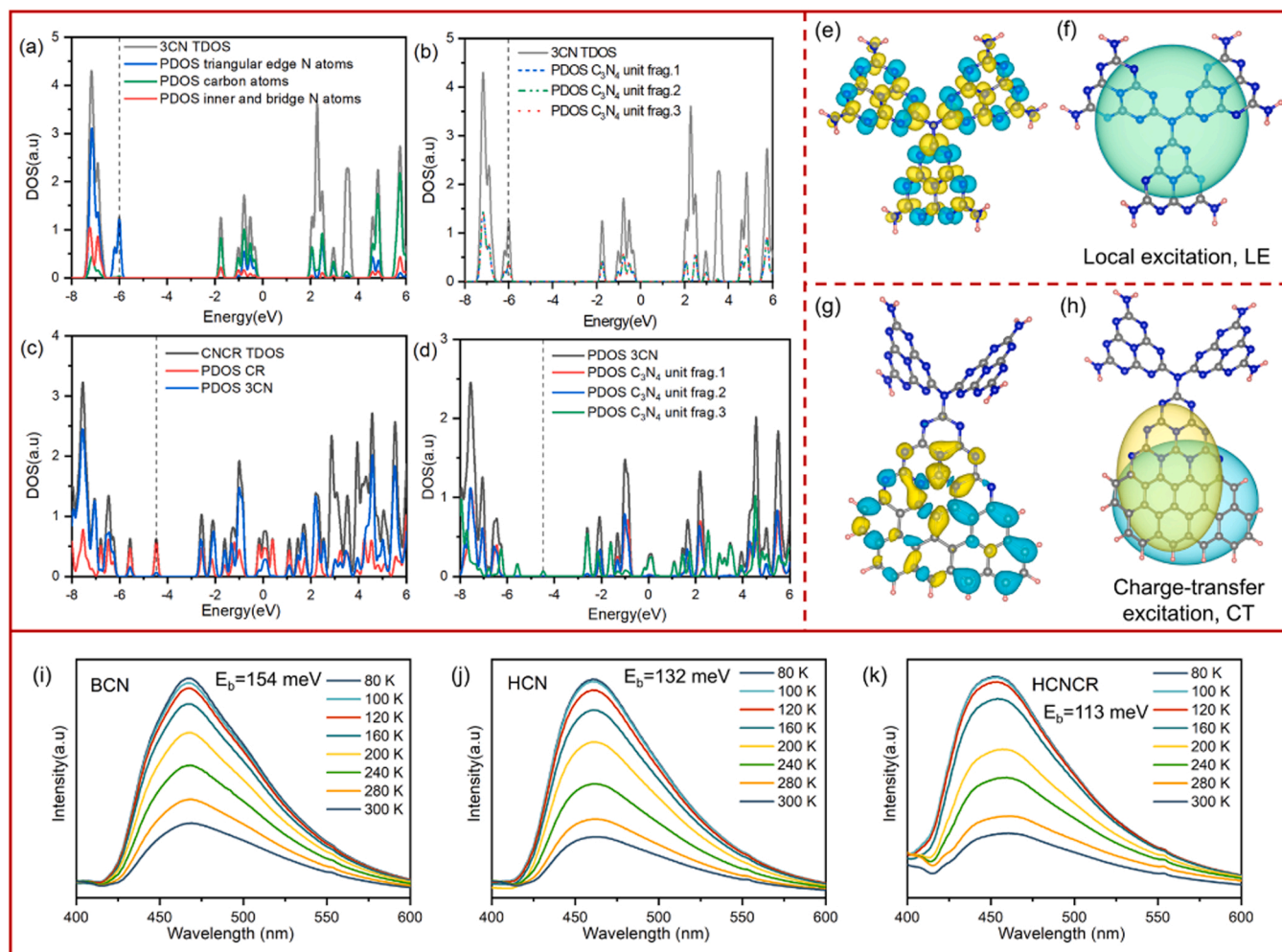
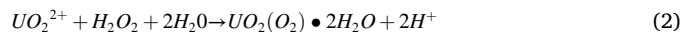


Fig. 3. (a–d) TDOS and PDOS of the model structure. (Each kind of atom and fragment are marked in Fig. S15, the broken line represents the position of HOMO). The CDD and graphical representation of D_{CT} for (e, f) 3CN and (g, h) CNCr (The blue and yellow distribution illustrate hole and electron depletion). Temperature-dependent PL spectra of (i) BCN, (j) HCN and (k) HCNCr.

three-dimensional direction is relatively similar. As for CNCr, two elliptical regions perpendicular to each other in space can be observed, confirming the good delocalization of holes and electrons in two different ways. The calculated D_{CT} of CN and CNCr are 0.002 Å and 1.897 Å. The above calculation results confirm the in-plane incorporated carbon ring induced the electronic excitation model of CN from local excitation (LE) to charge-transfer excitation (CT). Therefore, the calculated E_b gradually decreased (Table S6). The lower coulomb attractive energy results in more rapid dissociation of bound electron-hole pairs or excitons into free carriers, beneficial for the following charges migration. The exciton dissociation dynamics of samples were characterized by temperature-dependent PL spectra (TD-PL) to verify the calculated results. Fluorescence intensity gradually increases upon the temperature decreases, and the corresponding E_b can be obtained by fitting the Arrhenius equation [41], $I(T) = I_0 / (1 + A \exp(-E_b/k_B T))$. Accordingly, the estimated E_b decreased in the order of BCN (154 meV), HCN (132 meV), and HCNCr (113 meV) (Fig. 3i–k and S19), which stands the same trend with the theoretical calculations. The escalation of layer spacing induced by the thermally decomposing process has a positive effect on the dissociation of excitons. The advantages of carbon ring in the structure modulation are thus distinctly highlighted.

3.5. Photocatalytic mechanism toward uranium separation

For the sake of understanding the mechanism of photocatalytic U(VI) separation, the used photocatalyst was characterized. As displayed in Fig. 4a, a significant quantity of uniformly distributed microparticles can be observed on the surface of HCNCr. Based on the analysis of EDS, the microparticles belong to a kind of insoluble uranium oxide (Fig. S20). Then, the FT-IR and XPS analysis also confirm it. A new vibration band appears at 900 cm^{-1} , associated with the asymmetric stretching of $\text{U}=\text{O}$ (Fig. S21) [42]. Two XPS peaks locate at 392.84 eV and 382.04 eV attributed to U(VI) $4f_{5/2}$ and U(VI) $4f_{7/2}$ are observed after photoreaction (Fig. 4b). Finally, the crystal structure of the insoluble uranium is finalized by XRD as studtite ($(\text{UO}_2)(\text{O}_2) \cdot 2\text{H}_2\text{O}$) (Fig. 4c). Therefore, the generation of H_2O_2 during the photocatalytic reaction cannot be ignored. In 5% methanol solution, HCNCr establishes the highest H_2O_2 production activity, and the concentration of H_2O_2 reaches $54\text{ }\mu\text{mol/L}$ (Fig. 4d). We further investigated the concentration of H_2O_2 in the U(VI) involved photoreaction. Strangely, the concentration of H_2O_2 in the solution of the absent photocatalyst was higher than that of the contained photocatalyst (Fig. 4e), which means uranyl ions can generate H_2O_2 in the presence of light and methanol [26], and react with H_2O_2 to form studtite according to formula (2):



However, the concentration of U(VI) remains unchanged in the

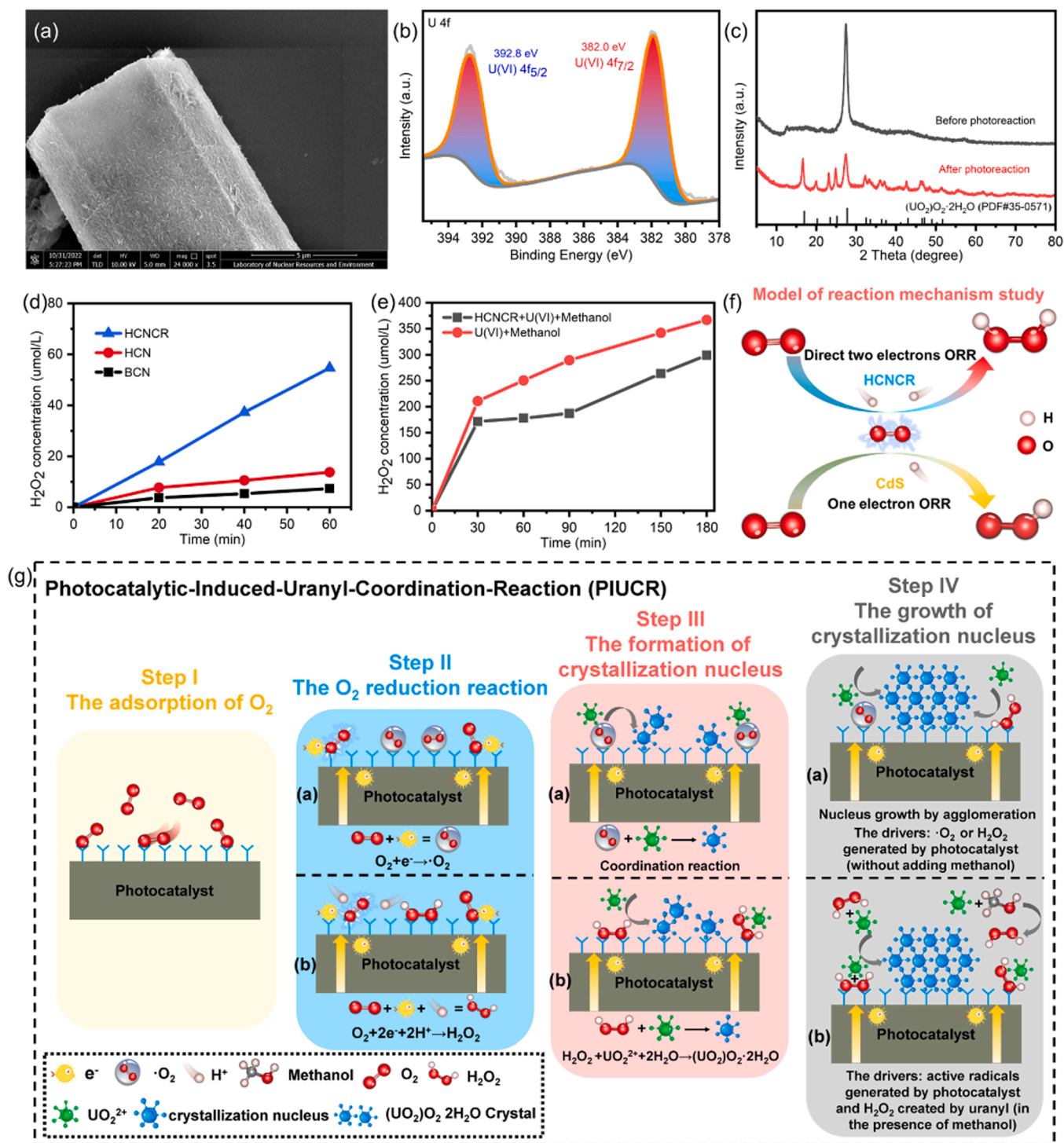


Fig. 4. (a) SEM image, (b) XPS spectrum of U 4f and (c) XRD pattern for the HCNCr after photoreaction. (d) the concentration of H₂O₂ produced by BCN, HCN and HCNCr in DI water (photocatalyst=10 mg, volume=50 mL, 5% methanol, pH=5.0). (e) the concentration of H₂O₂ in uranyl solution (C₀=50 mg/L, volume=50 mL, 5% methanol, pH=5.0). (f) The diagram of the model of reaction mechanism study. (g) The diagram of Photocatalytic-Induced-Uranyl-Coordination-Reaction (PIUCR). Step I, the adsorption of O₂. Step II, the O₂ reduction reaction (ORR) induced by photoelectrons, (a) one-electron ORR to form $\bullet\text{O}_2$ and (b) direct two-electrons ORR to form H₂O₂. Step III, the formation of crystallization nucleus induced by (a) $\bullet\text{O}_2$ and (b) H₂O₂. Step IV, the growth of crystallization nucleus in the force of (a) $\bullet\text{O}_2$ or H₂O₂ generated by photocatalyst (without adding methanol) and (b) H₂O₂ created by both photocatalyst and uranyl (in the presence of methanol).

absence of photocatalyst (Fig. S22). The above phenomena suggest that the photocatalyst has another special effect that allows uranium to be separated. According to previous studies [1], the final products of uranium after photoreaction are mainly made up of crystals UO₂ and studtite. The front product usually exists in anaerobic and reducing

conditions. In the N₂ protection, the XRD and XPS have confirmed that UO₂ was formed on the surface of HCNCr (Fig. S23). Considering that the final products are crystals, the crystallization nucleus must be created before the crystals appear. However, this process has not received attention in past studies, but it is the most prominent step in the

photocatalytic separation of uranium.

Firstly, after 1 h of light exposure, we turned the LED off and found that the separation of uranium continued with a separation rate as much as that of light condition (Fig. S24). Secondly, after illuminating the uranium solution for two hours, anatase titanium dioxide (TiO₂), and HCNCr were added and stirred in the dark. Interestingly, the uranium concentration slowly decreased while the concentration of H₂O₂ was correspondingly reduced (Fig. S25), and the color of the TiO₂ changed from white to yellow (Fig. S26). The XRD and XPS have confirmed studdite was formed on the surface of TiO₂ and HCNCr (Figs. S27 and S28). It is worth noting that the above separation reaction is related to the BET surface area and hydrophilicity of material, and the higher BET surface can promote the separation rate of U(VI) (Figs. S29–S32). Lastly, after adding NaHCO₃ to the reacted solution and adjusting the pH of the solution to 8, studdite rapidly dissolved to form uranyl ion, whereas the concentration of the uranium solution started to decrease and formed studdite again when the pH of the solution was adjusted to 4 (Fig. S33) [43].

As we can see from the above experiments, despite the direct reaction between UO₂²⁺ and H₂O₂, a substrate is necessary as a site for nucleation. After the nucleus is formed, the fuel for the aforementioned coordination reaction is the H₂O₂ produced by uranium (only for methanol-contained uranium solution). Finally, we summarized the essence of the photocatalytic uranium separation process, that is, photocatalyst adsorbs dissolved oxygen in water (Step I) and generates free radicals or H₂O₂ in the presence of photogenerated electrons (Step II), which further complex with U(VI) to form nucleus according to the coordination reaction (Step III). After that, seeds grow by agglomeration in the force of free radicals or H₂O₂ generated by photocatalyst or U(VI) (methanol condition) (Step IV), thus achieving solid-liquid separation. In a sentence, it can be called photocatalytic-induced-uranyl-coordination-reaction (PIUCR) (Fig. 4g). More experiments have been conducted to further prove the proposed PIUCR is reasonable and universal.

In the experimental study of photocatalytic separation of U(VI) in air atmosphere, the reduction of dissolved oxygen is inevitable, leading to the generation of •O₂ via single-electron reduction and H₂O₂ via two-electron reduction. To investigate the separate contributions of these two active species, we introduced CdS as the research subject. The sample characterizations of CdS are shown in Fig. S34. Nitro blue tetrazolium (NBT) is a common agent for detecting •O₂ [44]. The effect of •O₂ was investigated by CdS, a photocatalyst that generates •O₂ rather than H₂O₂ (Fig. S35), whereas the HCRCN generates H₂O₂ rather than •O₂ (Fig. 4f). As displayed in Fig. 5a, b, the photocatalytic degradation of NBT detected by HCNCr barely occurred, whereas plenty •O₂ was generated on the surface of CdS. The electron paramagnetic resonance (EPR) spectroscopy has also confirmed it. The typical characteristic signals for DMPO-•O₂ were markedly observed in CdS under light irradiation, which was absent in the HCNCr (Fig. S36), indicating the direct two-electron oxygen reduction reaction (ORR) in HCNCr. In the presence of U(VI), the separation rate of U(VI) by CdS was severely suppressed (Fig. S37), and the absorption peaks representing uranyl at the wavelength of 220 nm were not reduced significantly (Fig. 5d), whereas HCNCr exhibited the opposite experimental phenomenon to that of CdS (Fig. 5c). These experiments confirm both •O₂ and H₂O₂ have a positive impact on the U(VI) separation. However, the reaction mechanism of CdS is quite different from HCNCr in Step III. The coordination reaction was entirely achieved by •O₂ generated by CdS, rather than H₂O₂. Noteworthy, all the experiments about CdS were taken in the absence of methanol, where uranyl cannot generate H₂O₂ under light irradiation and no free radicals were generated (Fig. S38). The increased free radical yield in CdS-U(VI) may be attributed to the formation of heterojunctions between CdS and uranyl, accelerates the photocatalytic ORR.

The third step of PIUCR is the most critical and can be reflected in the following aspects. Firstly, after 20 min of CdS light exposure, turning off the light immediately stops the photocatalytic separation of U(VI),

which is completely opposite to HCNCr (Fig. S39). This indicates that the active substance for CdS photocatalytic separation of U(VI) is entirely provided by the •O₂ generated on the surface of CdS. Observation of the morphology of CdS after photocatalytic reaction through SEM reveals that small particle-shaped studdite is loaded on the surface of CdS (Fig. S40a–c). XRD and Raman spectra prove that it is an amorphous studdite (Fig. S40d, e). From the perspective of U(VI) separation, it is unnecessary for studdite crystals to grow, and the formation of a large amount of amorphous studdite can separate U(VI). Subsequently, COF-1 and COF-2 were used as photocatalysts under the same reaction conditions as HCNCr for photocatalytic separation of U(VI), and the results show that these two materials only achieved U(VI) separation after 1–2 h of light exposure, with even lower performance than when the light was not turned on (Fig. S41a). Through monitoring the changes in H₂O₂ concentration during the experimental process, it was found that the concentration of H₂O₂ in the solution was low during the initial hours of photocatalysis, indicating that these three materials can decompose H₂O₂ under light irradiation, and thus cannot form studdite on the surface (Fig. S41b). After a period of light exposure, the concentration of H₂O₂ in the solution increased, and only then did the uranium separation reaction occur, which is completely controlled by the fourth step of PIUCR. Based on the above analysis, it can be inferred that the third step of PIUCR is the most important step for photocatalytic separation of U(VI).

3.6. Surface reaction about adsorption and excitation of O₂

Therefore, DFT calculations were conducted to supply additional insights into the adsorption and excitation of O₂. The results confirm the formation of an endoperoxide species at the C2 and N6 positions of the triazine ring, as previously reported [45]. Furthermore, the calculated adsorption energy (*E*_{ads}) of −3.84 eV suggests that the triazine ring possesses superior adsorption capabilities for O₂ (Fig. 5g). As for CNCr, the O₂ is adsorbed on the junction of CN and carbon ring with a much lower *E*_{ads} (−4.66 eV) (Fig. 5h), where the position is also the electrons-rich reduction center and the site of most positive electrostatic potentials (Fig. S42). The two adsorption models show the “pull-electron” feature due to the stronger electrophilic ability of O₂. Thus, we further invested the transfer capability of electrons for both CN and CNCr. It can be observed that the adsorbed O₂ can draw more electrons (0.1033 e) transferring from the CNCr to O₂ than that of the CN (0.0387 e). This may be closely related to the delocalizability of the carbon ring according to the electron localization function (ELF). The closer the ELF approaches 0, the more pronounced the delocalization of electrons, whereas ELF = 1 represents the electrons are entirely localized. As shown in Fig. 5i, j, the electron around the O₂ molecule in CN is more localized than that of CNCr. Inversely, in the region of CNCr with lower ELF, the electron transfer between O₂ and CNCr is more likely to occur, which is consistent with the result of CDD. The above DFT analyses have confirmed the incorporation of the carbon ring provides a more feasible site for the adsorption of O₂ in thermodynamics, and promote the activation of O₂ in a three-dimensional space scale, which is vital for the uranyl coordination.

4. Conclusions

In summary, we have developed an extended electrons delocalized D-A polymeric heterojunction through the hybridization of CN and CR by virtue of sp² hybridized C–N bonds. The electronic excitation model of CN evolves from local excitation (LE) to charge-transfer excitation (CT) after forming the internal electric field by introducing carbon ring. Therefore, the exciton dissociation energy was reduced to 112 meV, the carrier lifetime was increased to 44.76 ns, and the photocatalytic performance was improved even under sunlight irradiation. With the in-depth investigation of the photocatalytic mechanism, we found that the essence of photocatalytic uranium separation is composed of two

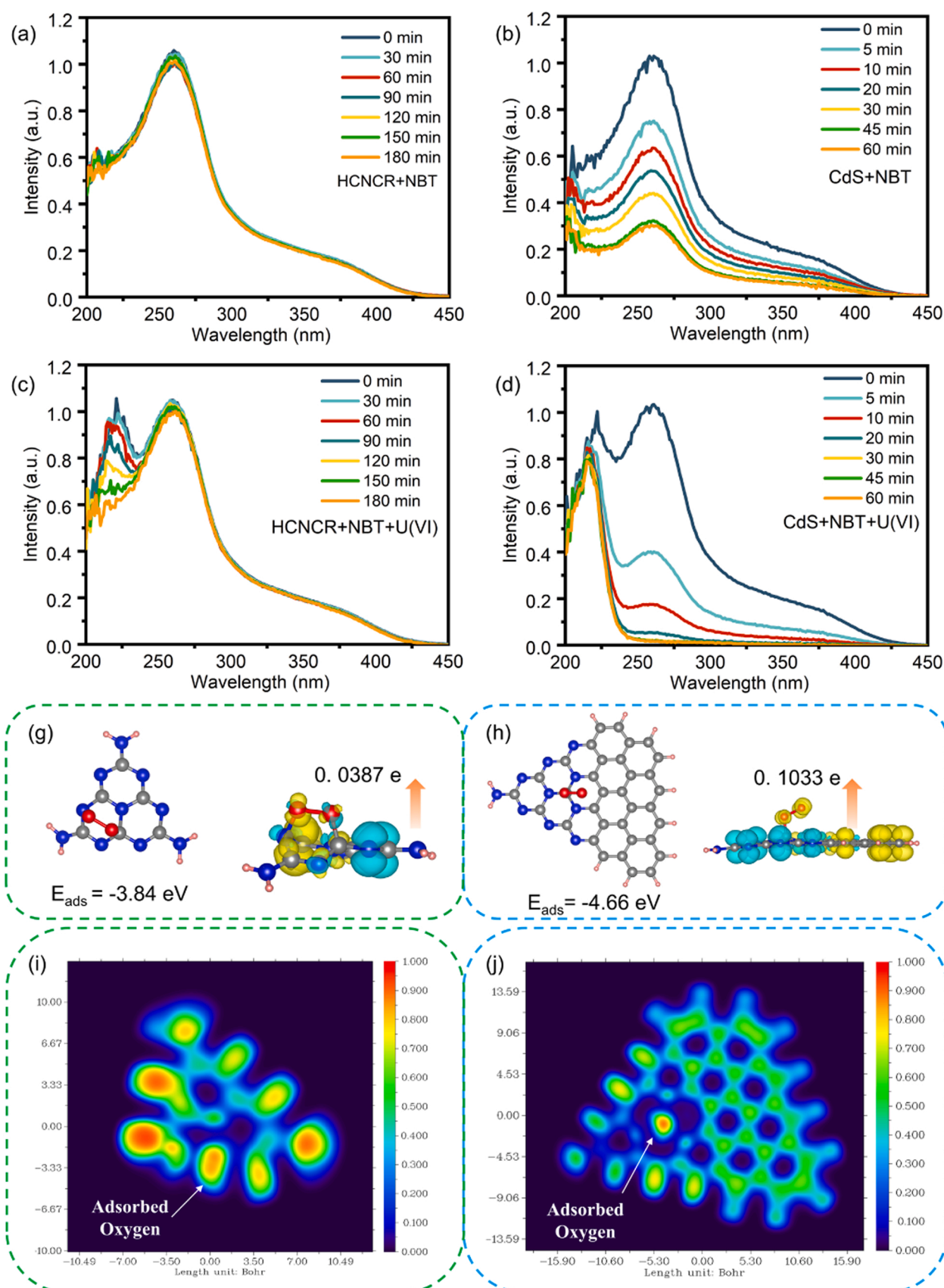


Fig. 5. Time-resolved absorption spectra of NBT of (a) HCNCr, (b) CdS (without adding methanol), (c) HCNCr and 50 mg/L U(VI), and (d) CdS and 50 mg/L U(VI) (without adding methanol). The adsorption energy and charge difference for the O_2 molecule adsorbed onto (g) CN and (h) CNCr. ELF diagram of the O_2 molecule adsorbed onto (i) CN and (j) CNCr.

parts: the formation of crystallization nucleus and the growth of crystallization nucleus. The carbon ring provides a more robust adsorption site for dissolved oxygen, while lowering the electron leaving domain around the dissolved oxygen, making it easier to be activated, which in turn promotes the formation of crystal nucleus. Most importantly, a new theory, photocatalytic-induced-uranyl-coordination-reaction (PIUCR), has been proposed to guide future research.

CRedit authorship contribution statement

Zifan Li: Conceptualization, Methodology, Investigation, Writing – review & editing. **Zhibin Zhang:** Resources, Funding acquisition, Supervision, Project administration. **Xiang Zhu:** Data analysis. **Cheng Meng:** Software, Validation, Project administration. **Zhimin Dong:** Funding acquisition, Validation. **Songtao Xiao:** Software, Validation. **Yingcai Wang:** Data analysis. **Youqun Wang:** Validation. **Xiaohong Cao:** Validation, Funding acquisition. **Yunhai Liu:** Resources, Funding acquisition, Supervision, Project administration.

Declaration of Competing Interest

The authors declare that they have no known competing financial interests or personal relationships that could have appeared to influence the work reported in this paper.

Data Availability

Data will be made available on request.

Acknowledgements

This work was financially supported by the National Natural Science Foundation of China (22066003, 22276030, U2167223, 22076022, 22206024), the Defense Industrial Technology Development Program (JCKY2019401C004). The temperature-dependent PL spectra were tested with the assistant of liquid nitrogen thermostat (LNT, JouleYacht, China).

Appendix A. Supporting information

Supplementary data associated with this article can be found in the online version at [doi:10.1016/j.apcatb.2023.122751](https://doi.org/10.1016/j.apcatb.2023.122751).

References

- [1] T. Chen, K. Yu, C. Dong, X. Yuan, X. Gong, J. Lian, X. Cao, M. Li, L. Zhou, B. Hu, R. He, W. Zhu, X. Wang, Advanced photocatalysts for uranium extraction: Elaborate design and future perspectives, *Coord. Chem. Rev.* 467 (2022), 214615.
- [2] H. Zhang, W. Liu, A. Li, D. Zhang, X. Li, F. Zhai, L. Chen, L. Chen, Y. Wang, S. Wang, Three mechanisms in one material: uranium capture by a polyoxometalate-organic framework through combined complexation, chemical reduction, and photocatalytic reduction, *Angew. Chem. Int. Ed.* 58 (2019) 16110–16114.
- [3] H. Li, F. Zhai, D. Gui, X. Wang, C. Wu, D. Zhang, X. Dai, H. Deng, X. Su, J. Diwu, Z. Lin, Z. Chai, S. Wang, Powerful uranium extraction strategy with combined ligand complexation and photocatalytic reduction by postsynthetically modified photoactive metal-organic frameworks, *Appl. Catal. B Environ.* 254 (2019) 47–54.
- [4] Y. Song, A. Li, P. Li, L. He, D. Xu, F. Wu, F. Zhai, Y. Wu, K. Hu, S. Wang, M. V. Sheridan, Unassisted uranyl photoreduction and separation in a donor–acceptor covalent organic framework, *Chem. Mater.* 34 (2022) 2771–2778.
- [5] M. Hao, Z. Chen, X. Liu, X. Liu, J. Zhang, H. Yang, G.I.N. Waterhouse, X. Wang, S. Ma, Converging cooperative functions into the nanospace of covalent organic frameworks for efficient uranium extraction from seawater, *CCS Chem.* 4 (2022) 1–14.
- [6] X. Jiang, Q. Xing, X. Luo, F. Li, J. Zou, S. Liu, X. Li, X. Wang, Simultaneous photoreduction of Uranium(VI) and photooxidation of Arsenic(III) in aqueous solution over g-C₃N₄/TiO₂ heterostructured catalysts under simulated sunlight irradiation, *Appl. Catal. B Environ.* 228 (2018) 29–38.
- [7] P. Li, Y. Wang, J. Wang, L. Dong, W. Zhang, Z. Lu, J. Liang, D. Pan, Q. Fan, Carboxyl groups on g-C₃N₄ for boosting the photocatalytic U(VI) reduction in the presence of carbonates, *Chem. Eng. J.* 414 (2021), 128810.
- [8] P. Li, J. Wang, Y. Wang, L. Dong, W. Wang, R. Geng, Z. Ding, D. Luo, D. Pan, J. Liang, Q. Fan, Ultrafast recovery of aqueous uranium: Photocatalytic U(VI) reduction over CdS/g-C₃N₄, *Chem. Eng. J.* 425 (2021), 131552.
- [9] Z.A. Lan, G. Zhang, X. Chen, Y. Zhang, K.A.I. Zhang, X. Wang, Reducing the exciton binding energy of donor-acceptor-based conjugated polymers to promote charge-induced reactions, *Angew. Chem. Int. Ed.* 58 (2019) 10236–10240.
- [10] Y. Hou, F. Liu, B. Zhang, M. Tong, Thiadiazole-based covalent organic frameworks with a donor-acceptor structure: modulating intermolecular charge transfer for efficient photocatalytic degradation of typical emerging contaminants, *Environ. Sci. Technol.* 56 (2022) 16303–16314.
- [11] Z. Wu, Z. Tong, Y. Xie, H. Sun, X. Gong, P. Qin, Y. Liang, X. Yuan, D. Zou, L. Jiang, Efficient degradation of tetracycline by persulfate activation with Fe, Co and O co-doped g-C₃N₄: performance, mechanism and toxicity, *Chem. Eng. J.* 434 (2022), 134732.
- [12] J. Fu, B. Zhu, C. Jiang, B. Cheng, W. You, J. Yu, Hierarchical porous O-doped g-C₃N₄ with enhanced photocatalytic CO₂ reduction activity, *Small* 13 (2017) 1603938.
- [13] B. Zhai, H. Li, G. Gao, Y. Wang, P. Niu, S. Wang, L. Li, A. Crystalline, Carbon nitride based near-infrared active photocatalyst, *Adv. Funct. Mater.* 32 (2022), e2207375.
- [14] Q. Zhang, X. Chen, Z. Yang, T. Yu, L. Liu, J. Ye, Precisely tailoring nitrogen defects in carbon nitride for efficient photocatalytic overall water splitting, *ACS Appl. Mater. Interfaces* 14 (2022) 3970–3979.
- [15] J. Zhang, T. Bai, H. Huang, M.H. Yu, X. Fan, Z. Chang, X.H. Bu, Metal-organic-framework-based photocatalysts optimized by spatially separated cocatalysts for overall water splitting, *Adv. Mater.* 32 (2020), e2004747.
- [16] L. Ni, T. Wang, K. Wang, J. Ma, Y. Wang, Novel control strategy for membrane biofouling by surface loading of aerobically and anaerobically applicable photocatalytic optical fibers based on a Z-scheme heterostructure Zr-MOFs/rGO/Ag₃PO₄ photocatalyst, *Environ. Sci. Technol.* 56 (2022) 6608–6620.
- [17] C. Wang, H. Zhang, W. Luo, T. Sun, Y. Xu, Ultrathin crystalline covalent-triazine-framework nanosheets with electron donor groups for synergistically enhanced photocatalytic water splitting, *Angew. Chem. Int. Ed.* 60 (2021) 25381–25390.
- [18] M.Z. Rahman, M.G. Kibria, C.B. Mullins, Metal-free photocatalysts for hydrogen evolution, *Chem. Soc. Rev.* 49 (2020) 1887–1931.
- [19] Y. Chen, M. Bhati, B.W. Walls, B. Wang, M.S. Wong, T.P. Senftle, Mechanistic insight into the photo-oxidation of perfluorocarboxylic acid over boron nitride, *Environ. Sci. Technol.* 56 (2022) 8942–8952.
- [20] P. Li, J. Wang, Y. Wang, J. Liang, D. Pan, S. Qiang, Q. Fan, An overview and recent progress in the heterogeneous photocatalytic reduction of U(VI), *J. Photochem. Photobiol. C* 41 (2019), 100320.
- [21] Z. Li, Z. Zhang, Z. Dong, F. Yu, M. Ma, Y. Wang, Y. Wang, Y. Liu, J. Liu, X. Cao, Y. Liu, Solar light-responsive CdS/Uio-66-NH₂ for ultrafast uranium reduction from uranium-containing mine wastewater without external sacrificial agents, *Sep. Purif. Technol.* 283 (2022), 120195.
- [22] Z. Wang, H. Liu, Z. Lei, L. Huang, T. Wu, S. Liu, G. Ye, Y. Lu, X. Wang, Graphene aerogel for photocatalysis-assist uranium elimination under visible light and air atmosphere, *Chem. Eng. J.* 402 (2020), 126256.
- [23] X. Gong, L. Tang, R. Wang, Z. Guo, P. Huang, L. Zhou, J. Zou, J. Lei, H. Liu, N. Li, X. Tang, W. Zhu, R. He, Achieving efficient photocatalytic uranium extraction within a record short period of 3 min by Up-conversion erbium doped ZnO nanosheets, *Chem. Eng. J.* 450 (2022), 138044.
- [24] Z. Zhang, Z. Li, Z. Dong, F. Yu, Y. Wang, Y. Wang, X. Cao, Y. Liu, Y. Liu, Synergy of photocatalytic reduction and adsorption for boosting uranium removal with PMo₁₂/Uio-66 heterojunction, *Chin. Chem. Lett.* 33 (2022) 3577–3580.
- [25] H. Wang, P. Mei, X. Huang, J. Xiao, Y. Sun, Uranyl(VI) boosting 3D g-C₃N₄ photocatalytic H₂O₂ production for U(VI) immobilization, *J. Clean. Prod.* 330 (2022), 129821.
- [26] Y. Hu, D. Tang, Z. Shen, L. Yao, G. Zhao, X. Wang, Photochemically triggered self-extraction of uranium from aqueous solution under ambient conditions, *Appl. Catal. B Environ.* 322 (2023), 122092.
- [27] Z. Wang, B. Li, H. Shang, X. Dong, L. Huang, Q. Qing, C. Xu, J. Chen, H. Liu, X. Wang, X.-G. Xiong, Y. Lu, Photo-induced removal of uranium under air without external photocatalysts, *Green. Chem.* 24 (2022) 7092–7099.
- [28] P. Xu, C.R. Zhang, Y.Z. Wu, L.H. Yuan, Y.H. Chen, Z.J. Liu, H.S. Chen, Fusing thienyl with N-annulated perylene dyes and photovoltaic parameters for dye-sensitized solar cells, *J. Phys. Chem. A* 124 (2020) 3626–3635.
- [29] T. Lu, F. Chen, Multiwfn: a multifunctional wavefunction analyzer, *J. Comput. Chem.* 33 (2012) 580–592.
- [30] Z. Liu, T. Lu, Q. Chen, An sp-hybridized all-carboatomic ring, cyclo[18]carbon: electronic structure, electronic spectrum, and optical nonlinearity, *Carbon* 165 (2020) 461–467.
- [31] X. Tang, L.S. Cui, H.C. Li, A.J. Gillett, F. Auras, Y.K. Qu, C. Zhong, S.T.E. Jones, Z. Q. Jiang, R.H. Friend, L.S. Liao, Highly efficient luminescence from space-confined charge-transfer emitters, *Nat. Mater.* 19 (2020) 1332–1338.
- [32] M. Shalom, S. Inal, C. Fettkenhauer, D. Neher, M. Antonietti, Improving carbon nitride photocatalysis by supramolecular preorganization of monomers, *J. Am. Chem. Soc.* 135 (2013) 7118–7121.
- [33] W. Che, W. Cheng, T. Yao, F. Tang, W. Liu, H. Su, Y. Huang, Q. Liu, J. Liu, F. Hu, Z. Pan, Z. Sun, S. Wei, Fast photoelectron transfer in C-CN plane heterostructural nanosheets for overall water splitting, *J. Am. Chem. Soc.* 139 (2017) 3021–3026.
- [34] Y. Yu, W. Yan, X. Wang, P. Li, W. Gao, H. Zou, S. Wu, K. Ding, Surface engineering for extremely enhanced charge separation and photocatalytic hydrogen evolution on g-C₃N₄, *Adv. Mater.* 30 (2018), e1705060.
- [35] P. Tan, Y. Deng, Q. Zhao, Temperature-dependent Raman spectra and anomalous Raman phenomenon of highly oriented pyrolytic graphite, *Phys. Rev. B* 58 (1998) 5435–5439.

- [36] Z. Dong, Z. Zhang, Z. Li, Y. Feng, W. Dong, T. Wang, Z. Cheng, Y. Wang, Y. Dai, X. Cao, Y. Liu, Y. Liu, 3D structure aerogels constructed by reduced graphene oxide and hollow TiO₂ spheres for efficient visible-light-driven photoreduction of U(VI) in air-equilibrated wastewater, *Environ. Sci. Nano* 8 (2021) 2372–2385.
- [37] S.S. Zade, N. Zamoshchik, M. Bendikov, From short conjugated oligomers to conjugated polymers. lessons from studies on long conjugated oligomers, *Acc. Chem. Res.* 44 (2011) 14–24.
- [38] M. Kou, Y. Wang, Y. Xu, L. Ye, Y. Huang, B. Jia, H. Li, J. Ren, Y. Deng, J. Chen, Y. Zhou, K. Lei, L. Wang, W. Liu, H. Huang, T. Ma, Molecularly engineered covalent organic frameworks for hydrogen peroxide photosynthesis, *Angew. Chem. Int. Ed.* 61 (2022), e202200413.
- [39] H. Wang, X. Sun, D. Li, X. Zhang, S. Chen, W. Shao, Y. Tian, Y. Xie, Boosting hot-electron generation: exciton dissociation at the order-disorder interfaces in polymeric photocatalysts, *J. Am. Chem. Soc.* 139 (2017) 2468–2473.
- [40] T. Le Bahers, C. Adamo, I. Ciofini, A qualitative index of spatial extent in charge-transfer excitations, *J. Chem. Theory Comput.* 7 (2011) 2498–2506.
- [41] W. Zhang, Z. Deng, J. Deng, C.-T. Au, Y. Liao, H. Yang, Q. Liu, Regulating the exciton binding energy of covalent triazine frameworks for enhancing photocatalysis, *J. Mater. Chem. A* 10 (2022) 22419–22427.
- [42] G. Cheng, A. Zhang, Z. Zhao, Z. Chai, B. Hu, B. Han, Y. Ai, X. Wang, Extremely stable amidoxime functionalized covalent organic frameworks for uranium extraction from seawater with high efficiency and selectivity, *Sci. Bull.* 66 (2021) 1994–2001.
- [43] K. Kim, D. Chung, H. Yang, J. Lim, E. Lee, K. Song, K. Song, A conceptual process study for recovery of uranium alone from spent nuclear fuel by using high-alkaline carbonate media, *Nucl. Technol.* 166 (2017) 170–179.
- [44] H. Wang, C. Yang, F. Chen, G. Zheng, Q. Han, A. Crystalline, Partially fluorinated triazine covalent organic framework for efficient photosynthesis of hydrogen peroxide, *Angew. Chem. Int. Ed.* 61 (2022), e202202328.
- [45] Y. Shiraishi, S. Kanazawa, Y. Sugano, D. Tsukamoto, H. Sakamoto, S. Ichikawa, T. Hirai, Highly selective production of hydrogen peroxide on graphitic carbon nitride (g-C₃N₄) photocatalyst activated by visible light, *ACS Catal.* 4 (2014) 774–780.